PAPER

Investigating the effect of transverse compressive loads on the electromagnetic performance of superconducting CORC® cables

To cite this article: Jiangtao Yan *et al* 2022 *Supercond. Sci. Technol.* **35** 115006

View the article online for updates and enhancements.

Investigating the effect of transverse compressive loads on the electromagnetic performance of superconducting CORC® cables

Jiangtao Yan[1,2] ⓘ**, Keyang Wang**[1,2] ⓘ**, Yuanwen Gao**[1,2,*] ⓘ**, Youhe Zhou**[1,2] **and Arend Nijhuis**[3,*] ⓘ

[1] Department of Mechanics and Engineering Science, College of Civil Engineering and Mechanics, Lanzhou University, Lanzhou, Gansu 730000, People's Republic of China
[2] Key Laboratory of Mechanics on Environment and Disaster in Western China, The Ministry of Education of China, Lanzhou University, Lanzhou, Gansu 730000, People's Republic of China
[3] University of Twente, Faculty of Science and Technology, 7522 NB Enschede, The Netherlands

E-mail: ywgao@lzu.edu.cn and a.nijhuis@utwente.nl

CrossMark

Abstract

High-temperature superconductor $(Re)Ba_2Cu_3O_x$ (ReBCO) conductor on round core cable (CORC®) has a large current carrying capacity for high field magnets. Lorentz forces acting on CORC conductors, cause a reduction of the critical current, or even permanent degradation of their performance when exceeding critical values. Transverse compressive stress is one of the principal mechanical stresses when CORC cables are bundled to cable-in-conduit conductors (CICC) conductors capable of operating at currents up to 100 kA in magnetic fields of up to 20 T. In this research, a mechanical-electromagnetic model is developed to study the effect of transverse compressive loads on the electromagnetic performance of CORC cables. A mechanical transverse load on the cable is implemented to simulate the electromagnetic force. A comparison of numerical simulations with experiments for a three-layer CORC cable is first performed to validate the model's reliability, with particular attention to critical current reduction during the transverse compression process. A novel feature of this paper is that the model developed can analyze both mechanical response under transverse compressive loads and electromagnetic performance under applied AC magnetic fields with low amplitudes. On this basis, the model investigates the effects of winding parameters on the axial strain and critical current reduction of the ReBCO layer in a single-layer CORC cable. The numerical analysis shows that increasing the winding angle can reduce the axial strain and critical current reduction of the ReBCO layer in the contact area. Subsequently, a detailed comparative study is carried out studying the axial strain of the ReBCO layer in the non-contact area with and without taking the winding core into account. In addition, a sudden increase in the magnetization loss is explained when the transverse compressive load reaches a certain level. Finally, a six-layer CORC cable's electromagnetic analysis is performed, and each tape layer's critical current reduction is investigated and discussed. The comparison of magnetization loss and current density between six- and single-layer CORC cables in the no-strain case is also given. This finite element model can guide optimizing a cable design for specific application conditions.

* Authors to whom any correspondence should be addressed.

(Some figures may appear in colour only in the online journal)

1. Introduction

With the rapid development of high-temperature superconducting (HTS) material technology, conductor on round core cable (CORC) cables made from $(Re)Ba_2Cu_3O_x$ (ReBCO) second-generation HTS tapes are expected to open opportunities to a new generation of large superconducting magnets with small size, high current density, high critical current, and low cooling cost. These large superconducting magnets can transfer high engineering current density in background magnetic fields exceeding 20 T, which extends the application of CORC cables for high field magnets [1–3]. Due to the high-field magnets' extreme operation conditions, CORC cables have to withstand extreme stress and strain caused by the interaction of current and high magnetic field [4]. In the case of some very high fields, CORC cables are susceptible to plastic damage and deformation by Lorentz forces [5–7].

The mechanical and electromagnetic response of CORC cables has attracted significant attention because of their importance for magnet design and optimization [8–22]. Anvar *et al* [8] presented finite element (FE) modeling of the stress–strain state of CORC cables and wires under bending loads. They optimized the parameter variables (winding angle, tape width, tape thickness, etc) to improve the mechanical properties of CORC cables. Subsequently, analytical and FE models were also developed to predict the performance of CORC wires under axial tensile strain [9]. Wang *et al* [10] investigated the nonlinear contact behavior of the CORC cable from theoretical and FE perspectives, and a formula for estimating the contact force was proposed. They evaluated the performance of CORC cables under axial tensile loading. ReBCO layer strains, interlayer interactions, contact pressure, and friction were calculated [11]. Van der Laan *et al* [12] tested optimized CORC cables and wires for axial tensile loading. They found that the irreversible strain limit of the optimized CORC cables and wires could be ten times higher than that of single ReBCO tape with the irreversible strain limit reaching up to even 7%. These studies have only investigated CORC cable from a mechanical point of view that lacked electromagnetic analysis.

Mulder [13] measured the critical characteristics of CORC cables after winding them into magnet coils. They found that the strain level of the superconducting tape in CORC cables exceeded its irreversible strain limit when the winding radius is small, resulting in significant degradation of the overall cable performance. Van der Laan *et al* [14] investigated the effect of monotonic and cyclic axial tensile loading on the critical current degradation of CORC cables. Solovyov *et al* [15] experimentally tested the AC loss characteristics of single-layer CORC cables. They found that the helical structure of CORC cables reduces the AC loss compared to straight superconducting tapes. Sheng *et al* [16] developed a numerical model to calculate the magnetization loss of CORC cables under a transverse magnetic field based on the *H*-formulation [23, 24]. In 2019, Wang *et al* [17] calculated the electromagnetic characteristics of single- and three-layer CORC cables in transverse magnetic fields by the *T–A* formulation [25–27]. They pointed out that the lower magnetization loss in CORC cables, compared to straight superconducting tapes, was due to the lower surface-induced currents caused by the tape's spatial distribution in the helical structure. Two adjacent induced current loops will interact and reduce the induced current amplitude. In addition, also due to the magnetic shielding effect, the magnetization loss per superconducting tape decreases as the number of wound layers increases [17]. Recent studies [18–21] have also analyzed the electromagnetic behavior of CORC cables in multiple aspects. Wu *et al* [18] investigated the electromagnetic and mechanical properties of single-layer CORC cables with and without shielding currents. Clegg *et al* [19] discussed in depth the distribution of critical current and critical current density in multiple tapes of CORC cables by a three-dimensional (3D) FE method. Li *et al* [20] proposed a modified *T–A* formulation to calculate the losses of cables under different electrical and thermal conditions. Fareed *et al* [21] conducted a comprehensive study on the twist pitch angle of CORC cables. The optimum pitch was determined from the perspective of AC loss. To our knowledge, it has not been examined before how mechanical transverse load, simulating the electromagnetic force on a CORC cable under the influence of an applied AC magnetic field, affects magnetization loss.

Due to the interaction of current and magnetic fields, transverse compressive stress is one of the principal mechanical stresses that CORC cables have to withstand in operating conditions. The transverse compressive stresses acting on a cable or strands leading to irreversible degradation of the critical current and reducing the current sharing temperature have been significant issues in developing low-temperature-superconducting (LTS)-based CICC conductors for thermonuclear experimental reactor (ITER) [28]. Significant degradation occurred in one of the two CORC-CICC samples tested at the SULTAN facility of the Paul Scherrer Institute in Switzerland. The degradation of one of the 6-around-1 conductors may result from the deformation of the CORC cables due to the cable configuration and winding parameters [13]. Thus, optimizing CORC cables is essential to avoid degradation caused by transverse compression. Van der Laan *et al* [22] experimentally investigated the effect of transverse monotonic and cyclic mechanical loading on the critical performance of CORC cables. Their work focused on the critical current degradation, not on the magnetization loss. Except [22], few works

are conducted for CORC cables for analyzing the electromagnetic performance when subjected to transverse compressive loads.

In this paper, we study the mechanical and electromagnetic properties of CORC cables under transverse compressive loads. The 3D model built can provide a platform for optimizing the winding parameters of CORC cables. First, in section 2, the 3D mechanical-electromagnetic model is described. Then, in section 3, the results of mechanical and electromagnetic simulations of single- and six-layer CORC cables are discussed. The main conclusions of this work are summarized in section 4.

2. Model description

Here, we consider multilayer CORC cables under transverse compression, as shown in figure 1. The ReBCO tapes are SCS2030 tapes from SuperPower Inc. The winding angle of each layer is α_i. The width of the tape is w, and the applied AC magnetic field amplitude is B. The load and the AC magnetic field are applied both to the CORC cable in the transverse direction, and the direction of the load with respect to the AC magnetic field is perpendicular. The main geometric and mechanical parameters of the CORC cable are listed in table 1.

2.1. Main steps and implementation

The work on CORC cables [8–22] is either treating the mechanical, electromagnetic, or critical transport characteristics, lacking a model so far that simultaneously handles mechanical and electromagnetic properties. Consequently, a 3D numerical model of the CORC cable is established based on the *T–A* formulation and the FE method. The detailed process is divided into a mechanical deformation module and an electromagnetic analysis module, see figure 2.

First, the entire tape is considered a homogenized volume. The axial strain is calculated for the superconducting tape after deformation in the body coordinate system using the coupled solid mechanics module and the flow method module.

Second, the ReBCO layers in the original cable structure are created using the shell unit module. The shell cell is created to locate the ReBCO layer in the tape accurately. When the cable is deformed, the mechanical response of the ReBCO layer in each superconducting tape is determined by mapping the data acquired in the first step into the shell unit.

Lastly, the cylindrical shape of the air domain is applied, and the electromagnetic characteristics are calculated using the partial differential equation module coupled with the magnetic field module.

It is worth noting that the step shown in figure 2 is the mechanical loading process first, and then the electromagnetic analysis is performed after the end. It means there is no coupling relationship between step-1 and step-2. Next, we detail the implementation of the mechanical and electromagnetic processes.

2.2. 3D mechanical model

A 3D mechanical model with appropriate boundary conditions is developed in COMSOL Multiphysics® software [31] to evaluate the deformation of the superconducting tape ReBCO layer under transverse compressive loading. The detailed FE model is shown in figure 3. The ReBCO layer faces the winding core.

The CORC cable is fully constrained at both terminals, and the displacement boundary conditions for different operating conditions are imposed to simulate electromagnetic forces. The coefficient of friction between all contact pairs in the simulation is 0.3. The number of seeds set along the width and thickness directions of the tape is 20 and 1, respectively. The unit size in the length direction of the tape is kept consistent with the width direction, i.e. when the size of the unit is $0.1015\,\text{mm} \times 0.1015\,\text{mm} \times 1\,\text{mm}$, the mesh converges better.

Establishing a body coordinate system in the axial direction of the superconducting tape during the whole cable deformation process is required to acquire the overall performance of the CORC cable. This is difficult for the axial direction of the deformed cable in the simulation but in order to achieve this, here, an equivalent method is used. The helical superconducting tape is considered a fluid channel, supposing that an ideal incompressible fluid flows through the structure of the deformed cable. Without consideration of the boundary effect, the velocity direction of the fluid flow can be regarded as the axial direction of the superconducting tape. The fluid is set to flow uniformly without inertial and volumetric forces in the calculation. The control equation can therefore be simplified as

$$\nabla \cdot \mathbf{u} = 0. \tag{1}$$

$$\nabla \cdot \ [-p\mathbf{I} + \mathbf{K}] = 0. \tag{2}$$

Here $\mathbf{u}$ is the deformation velocity tensor, p is the pressure intensity, $\mathbf{I}$ is the unit matrix, the deviation tensor of stress $\mathbf{K} = \mu\,(\nabla\mathbf{u} + (\nabla\mathbf{u})^{\text{T}})$, and μ is the dynamic viscosity. The boundary conditions are set for one end of the CORC cable as the inflow port, the other end as the flow outlet, and the outlet pressure is zero. In this way, after determining the axial direction of each point on the superconducting tape, the axial strain $\varepsilon_{\text{axial}}$ at each point can be obtained as follows:

$$\varepsilon_{\text{axial}} = \varepsilon_{\text{cable}} \cdot \frac{\mathbf{u_p}}{|\mathbf{u_p}|} \tag{3}$$

where $\mathbf{u_p}$ is the deformation velocity tensor at any point on the tape, $\varepsilon_{\text{cable}}$ is the strain of the CORC cable.

The above steps map the CORC cable's strain after loading deformation to the ReBCO layer, and the obtained strain will be applied to the subsequent electromagnetic analysis.

2.3. 3D electromagnetic model based on T–A formulation

The *T–A* formulation is used to calculate the current and magnetic field. A current vector potential $\mathbf{T}$ is defined [25, 32, 33]:
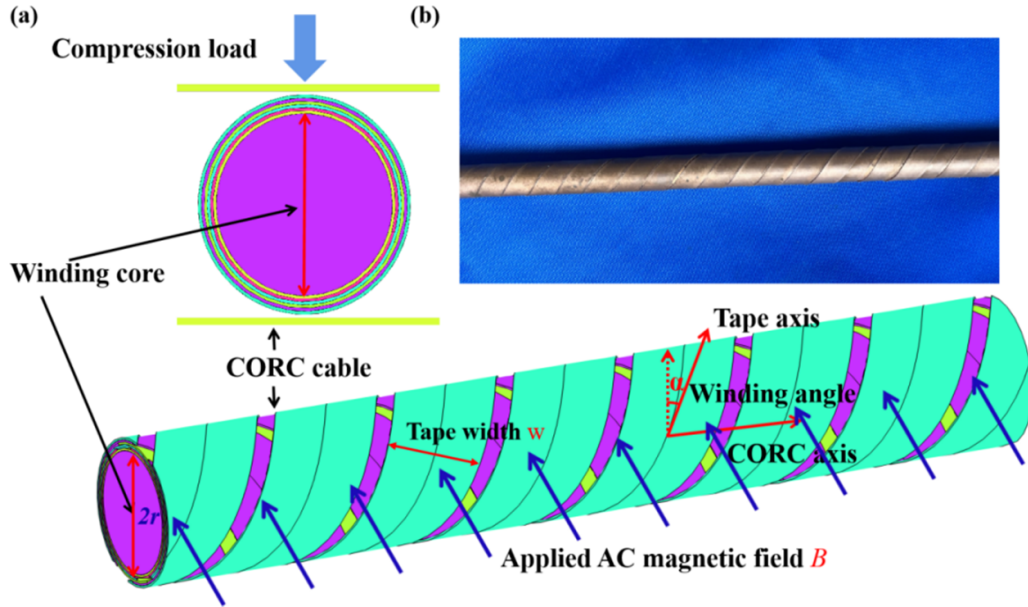
Figure 1. (a) Geometry of the CORC cable transverse compression model and (b) the structure of a multilayer CORC cable.

Table 1. Geometric and mechanical parameters of the CORC cable.

Parameters		Value
Former size ($2r$)	(mm)	2.58
Tape width (w)	(mm)	2.03
Tape layers	(—)	1, 6
Winding angle (α_i)	(°)	31–70
Number of tapes per layer	(—)	2
Winding core (Young's modulus)	(GPa)	130 [29]
Winding core (Poisson ratio)	(—)	0.3
HTS tape (Young's modulus)	(GPa)	180 [30]
HTS tape (Poisson ratio)	(—)	0.3

$$\mathbf{J} = \Delta \times \mathbf{T} \tag{4}$$

where $\mathbf{J}$ is the current density. The controlling equation of Faraday's law is

$$(\Delta \times \mathbf{E}) \cdot \mathbf{n} = \frac{-\partial B_n}{\partial t}. \tag{5}$$

Here, $\mathbf{n}$ stands for the tape's unit normal vector. B_n denotes the normal component of the magnetic field $\mathbf{B}$. The current density $\mathbf{J}$ determines the electric field $\mathbf{E}$. And the $\mathbf{E}$–$\mathbf{J}$ relationship for the REBCO conductor is expressed as [34, 35]

$$\mathbf{E}(\mathbf{J}) = E_0 \left(\frac{|\mathbf{J}|}{J_c(\mathbf{B})} \right)^n \frac{\mathbf{J}}{J_c(\mathbf{B})} \tag{6}$$

where the critical electric field $E_c = 1 \times 10^{-4}$ V m^{-1} and the flux-creep exponent $n = 43$ [36]. $J_c(\mathbf{B})$ with a field-dependent critical current density is described as [35]

$$J_c(\mathbf{B}) = J_c(B_{par}, B_{per}) = \frac{J_{c0}}{\left[1 + \sqrt{(kB_{par})^2 + B_{per}^2}/B_c \right]^b} \tag{7}$$

where B_{par} and B_{per} denote the magnetic field components parallel and perpendicular to the tape surface, respectively, J_{c0} is the critical current density. k, b, and B_c are shape parameters describing the anisotropic characteristics of the REBCO conductor, and $k = 0.009\ 13$, $b = 0.7518$, and $B_c = 467.4$ mT [34].

Equation (8) is used to calculate the normalized critical current of the ReBCO layer. The critical current of the ReBCO layer is thought to be determined by the tape's weakest section [37]:

$$\frac{J_c}{J_{c0}} \begin{cases} 1 - a|\varepsilon_i|^n, & \varepsilon_i < 0.45\% \\ 0, & \varepsilon_i \geqslant 0.45\% \end{cases}. \tag{8}$$

ε_i is the intrinsic strain in the ReBCO layer after the transverse compression load is applied to the cable, which can be obtained by equation (3). A single straight tape experiment determined the strain sensitivity parameters a and n. Particular attention should be paid to the fact that the power-law expression in equation (8) is only valid for 77 K, self-field conditions and small applied magnetic fields and cannot be used for larger applied magnetic fields. There is no consideration of a DC applied magnetic field in this study and in the experimental measurements of a and n.

The magnetization loss energy induced in the superconducting layer is calculated by [38–42]:

$$Q = 2 \int_{1/(2f)}^{1/f} dt \int_{\Omega} \mathbf{E} \cdot \mathbf{J} d\Omega \tag{9}$$

where Q is in units of J/cycle, and $1/f$ is the period of the applied background sinusoidal magnetic field.
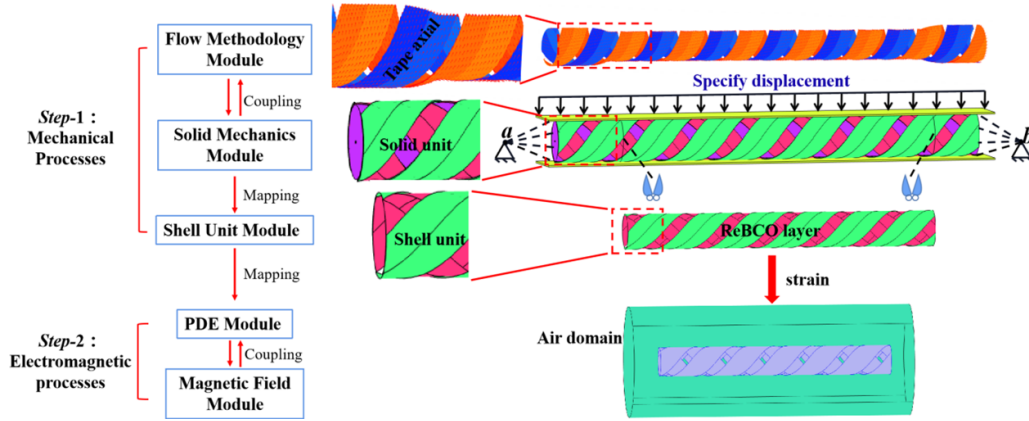
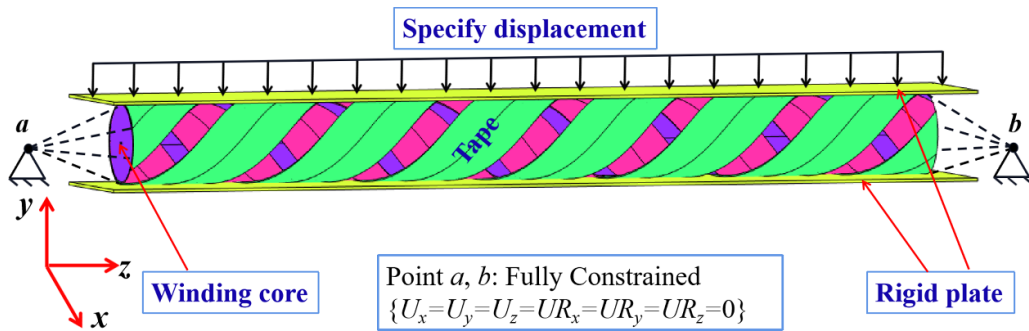**Figure 2.** Schematic diagram of the mechanical-electromagnetic model.

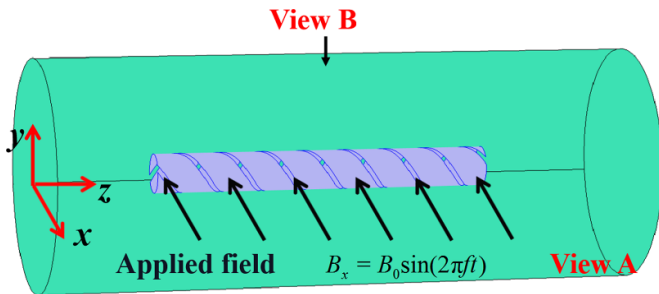**Figure 3.** A FE model for structural analysis of double-layer CORC cables.

Figure 4. Schematic illustration of views A and B and applied field.

A Dirichlet–Neumann boundary condition is imposed on the outer boundary of the 3D air domain to simulate the applied background magnetic field (see figure 4):

$$\mathbf{B} = ((B_0 \sin(2\pi f t) \; 0 \; 0) \tag{10}$$

where B_0 is the magnitude of the AC magnetic field, f is the frequency.

3. Results and discussion

3.1. Model validation

The change of the critical current or its reduction is calculated and compared with [22] to validate the above mechanical-electromagnetic models. The choice of geometric and physical properties is in accordance with [22]. The ReBCO tape is surrounded by a 20 μm thick plated copper layer. The CORC cable comprises nine tapes wound into three layers on a solid stainless-steel former with a diameter of 4.92 mm. The spacing between the CORC cable tapes is 0.5 mm and more details are reported in [22]. Figure 5 compares the critical current reduction from the experimental test and the simulation. Exp-1 and Exp-2 represent the critical current reduction data measured twice under the same experimental conditions for the same type of CORC cable samples. The load where the normalized critical current becomes less than 95% is taken as the critical load in the experiment. The 95% criterion refers to the critical current reduction of the cable as a whole, possibly with local irreversible reduction already occurring. The authors do not claim this threshold to be a relevant criterion, it is just considered here for comparison with the reported experiments. We find that the critical load obtained from the simulation amounts to 130 kN m^{-1} and from the experiment 245 and 208 kN m^{-1} is reported for Exp-1 and Exp-2, respectively. The differences between the simulation results and Exp-1 and Exp-2 are 47% and 38%, respectively. In order to analyze if our model itself causes this relatively large difference, simulations of the critical current reduction under axial tensile loading were performed. Compared to transverse compression, the tape strain obtained in the case of axial tension is far more uniform.
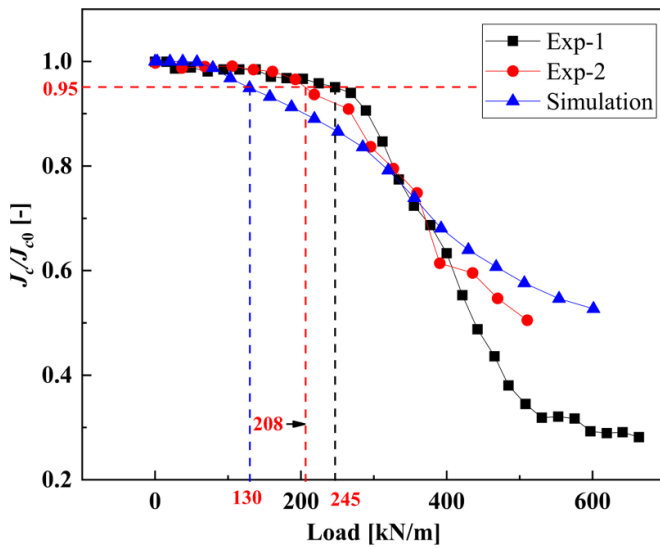
Figure 5. Experimental and simulated results of the critical current reduction and degradation under transverse mechanical load.
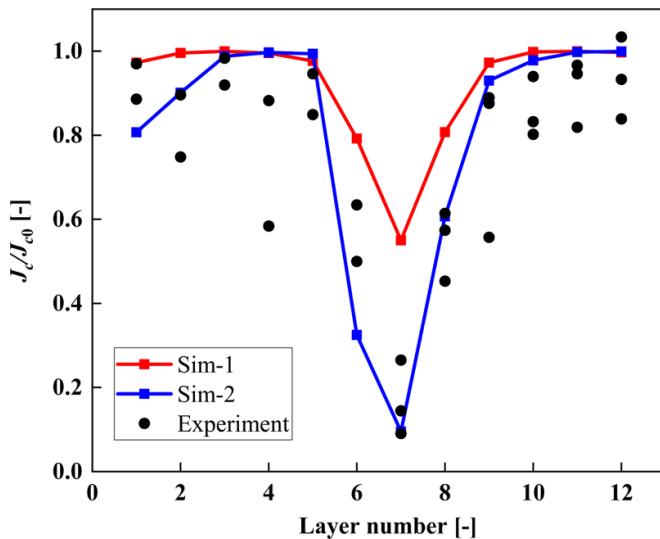

Figure 6. The dependence of critical current reduction on applied tensile strain measured in CORC®-S30 is compared between experiment and two simulations.

Figure 6 shows the experimental and simulation results of the critical current reduction for different layers of CORC®-S30 under axial tensile loading. Specific details about CORC®-S30 are described in [14] and similar results have been reported previously in [9]. Sim-1 represents the data obtained by averaging the tape strain as a whole and substituting it into equation (8), while the data of Sim-2 are obtained directly using equation (8). From figure 6, it can be seen that the direct use of equation (8) to solve for the critical current reduction value agrees reasonably well with the experiment, which also indicates that it is acceptable to use equation (8) to solve for the critical current reduction in our model for axial strain.

After verifying the method for solving the critical current reduction, the other causes are analyzed. One of the reasons

for the difference may be explained in [43]. The critical properties of a single superconducting tape in axial tension, transverse compression, and torsion are studied in detail in [43]. It is pointed out in [43] that the area where the axial strain of the tape is greater than 0.45% is defined as the 'damaged area'. The critical current starts to reduction only when the damaged area is 15%–20% of the tape width [43]. It can be noted that the 15%–20% difference also relies on the chosen electric field criterion. A criterion of 10 μV m^{-1} was utilized in [43], while 100 μV m^{-1} was employed experimentally here and in [22]. The higher electric field makes the experimental method less sensitive than the model for detecting initial reduction. Even with the improved new method (I_c-integration method), there is still a 21% difference between the FE and experimental results for SCS4050 tapes in [43]. Considering that the complex structure of the CORC cable compared to a single superconducting tape (with dog-boning being ignored here), combined with the influence of interlayer interactions for transverse load, it is reasonable to expect an error between our model and experimental results. Furthermore, the soldered terminations and contact resistance between the tapes may be another reason for the larger critical load found in the experiment. In practice, the current redistribution among three tapes of the same layer of the CORC cable mainly depends on the conductor resistance and terminal contact resistance [44]. Current redistribution depends mainly on the terminal contact resistance when the terminal contact resistance is high. When the terminal contact resistance is low enough, current redistribution will be limited by the tape critical current. Similarly, it has been demonstrated in [45] that the tape-to-tape contact resistance plays a critical role in the cable's current sharing capability and current distribution. The presence of contact conductance leads to current sharing, which lifts the decrease of the overall cable critical current density.

Although there is a difference between our model and the experimental results, our model can make reasonable quantitative predictions of the mechanical-electromagnetic behavior under transverse compressive loading, explaining at least qualitatively the impact of the cable geometry parameters.

3.2. Single-layer CORC cable under transverse compression

The core and the winding angle of the tape are critical components of the CORC cable, and it is meaningful to study their effect on its properties. First, the impact of the winding angle on the transverse compression properties of CORC cables is considered.

Figure 7 shows that the axial strain distribution of the ReBCO layer of single-layer CORC cable is periodic (strain output along the ReBCO layer winding direction). Therefore, we take one period at different winding angles for the subsequent comparison. According to the rainbow lines in figure 7, the axial strain in the ReBCO layer can be roughly divided into three parts: the larger positive strain region, the larger negative strain region, and the smaller strain region. The transition of axial strain in these three regions is sharp. In combination with the cloud diagram of the ReBCO layer, it can be
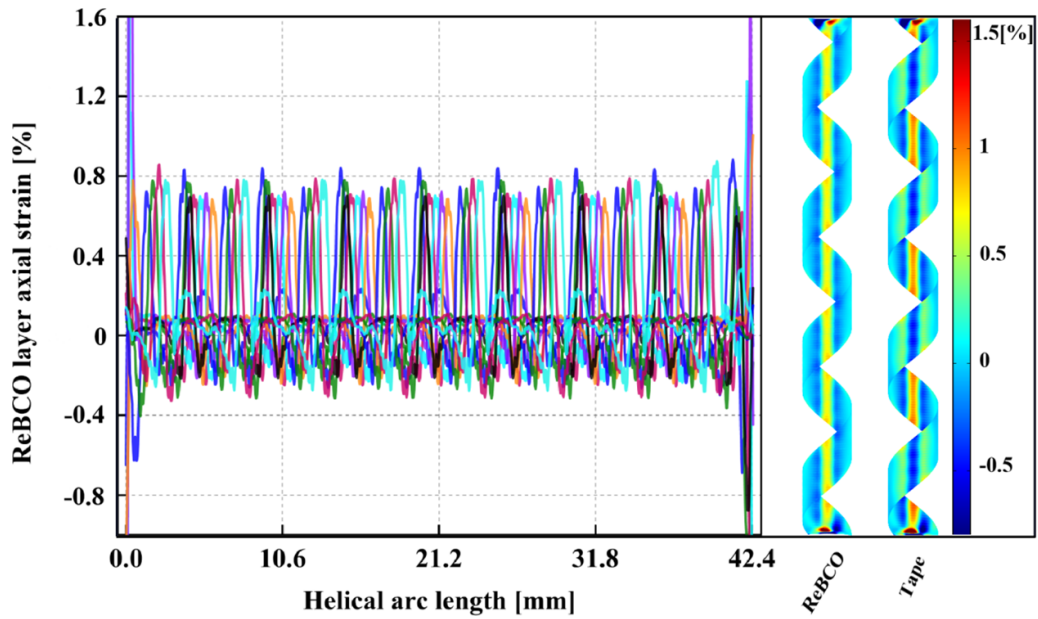
Figure 7. Axial strain of ReBCO layer at 40° winding angles after 5.41% transverse compressive strain of single-layer CORC cable.
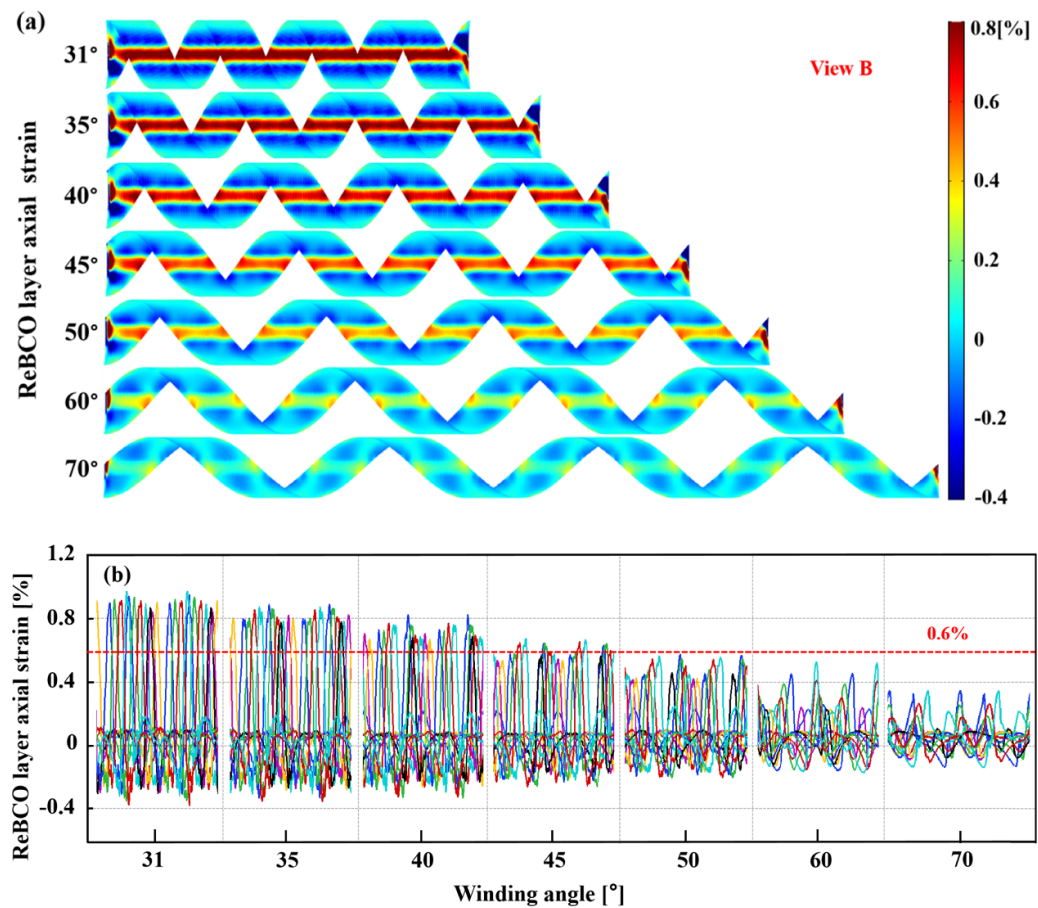

Figure 8. Axial strain of ReBCO layer with winding angle after transverse compressive strain of 5.41% for single-layer CORC cable.

seen that the larger positive and larger negative strains are located where the CORC cable comes into contact with the rigid plane. In contrast, the smaller strain region is located where the CORC cable does not come into contact with the rigid plane.

Figure 8 depicts the axial strain of the ReBCO layer versus the winding angle for a single-layer CORC cable after a transverse compressive strain of 5.41%. All references to transverse compression strains here, including those that follow, refer to
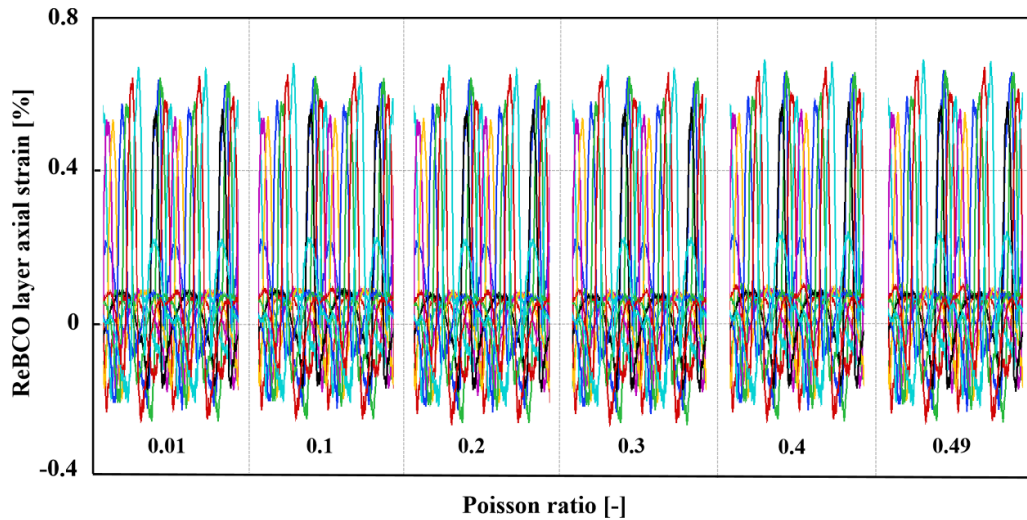
Figure 9. Axial strain of ReBCO layer with winding angle after transverse compressive strain of 5.41% for single-layer CORC cable.

the engineering strains at the downward compression distance. Here we define the area in contact with the rigid plate as the contact area and the other areas as the non-contact area. It can be seen from figure 8 that the ReBCO layers' axial strain is larger in the contact area and decreases with the increase of winding angle. The reason is that the smaller the winding angle of the CORC cable, the smaller the gap between the tapes. The tape mainly carries the effect of transverse load, and as the winding angle increases, the gap between the tapes increases, and part of the transverse load effect is carried by the winding core. This suggests that choosing a larger winding angle in winding CORC cables can improve the ReBCO layer strain limit. Except for the end effect, the axial strain in the ReBCO layer of the contact area is larger on the tape's edge and relatively flat in the middle, as shown in figure 8(a). The higher strain at the edge of the tape can be explained by the bending deformation of the tape due to the transverse compression load. Additionally, figure 8(b) shows that when other conditions are kept constant, the axial strain of the ReBCO layer in the non-contact region does almost not change with the winding angle.

The effect of Poisson's ratio of the core material and the radius of the core on the transverse compression properties of the single-layer CORC cable is then studied. Figure 9 shows the effect of different core Poisson's ratios on the axial strain of the ReBCO layer with a winding angle of 45. The axial strain of the ReBCO layer at the contact area is almost unaffected by the core Poisson's ratio variation. There is also almost no effect on the ReBCO layer axial strain at the contact area by changing only the core diameter when other conditions are kept constant (not shown here).

3.3. Electromagnetic analysis of single-layer CORC under transverse compression

3.3.1. Critical current reduction of single-layer CORC cables.
In the previous section, the axial strain distribution of the ReBCO layer is calculated in the CORC cable under transverse

compressive loading. According to equation (8), the critical current reduction of the ReBCO layer is solved by mapping the results of the mechanical deformation module.

Figure 10 illustrates the critical current reduction of the ReBCO layer against winding angle for a single-layer CORC cable following a 5.41% transverse compressive strain. The critical current reduction of the ReBCO layer is mainly concentrated in the contact area, especially at the edge of the tape, and it reduces with the increase of the winding angle. It is the opposite of what is observed for the tensile case, where the critical current reduction increases with the increase of the winding angle [9]. Therefore, to optimize the winding parameters of the CORC cable, both axial tension and transverse compression cases should be considered depending on its application.

The critical current reduction of the ReBCO layer is largest at the winding angle of 31. For winding angles larger than 50, the critical current of the ReBCO layer is (practically) not reduced. This can be attributed to the fact that the axial strain of the ReBCO layer at the contact area reduces with the increase of the winding angle. The irreversible critical strain in the ReBCO layer of the CORC cable is 0.6% [22], considering a thermal strain of −0.15% during transverse compression. Since the axial strain of the ReBCO layer in the contact area at a winding angle of 50 is practically less than 0.6% (see figure 8(b)), the critical current is not reduced.

Figure 11 show the axial strain distribution and critical current reduction characteristics of the ReBCO layer in CORC cables with 31 and 50 winding angles at different transverse compressive strains. The critical current of the ReBCO layer of the 31 winding angle CORC cable shows irreversible reduction at transverse compressive strain exceeding 2.77%, as shown in figure 11(a). The critical current of the ReBCO layer did not show any significant reduction for the 50 winding CORC cable, even when the transverse compressive strain was over 5.41%, as shown in figure 11(b). Consequently, tape wound at a larger angle can lead to a better performance in terms of critical current for transverse load.
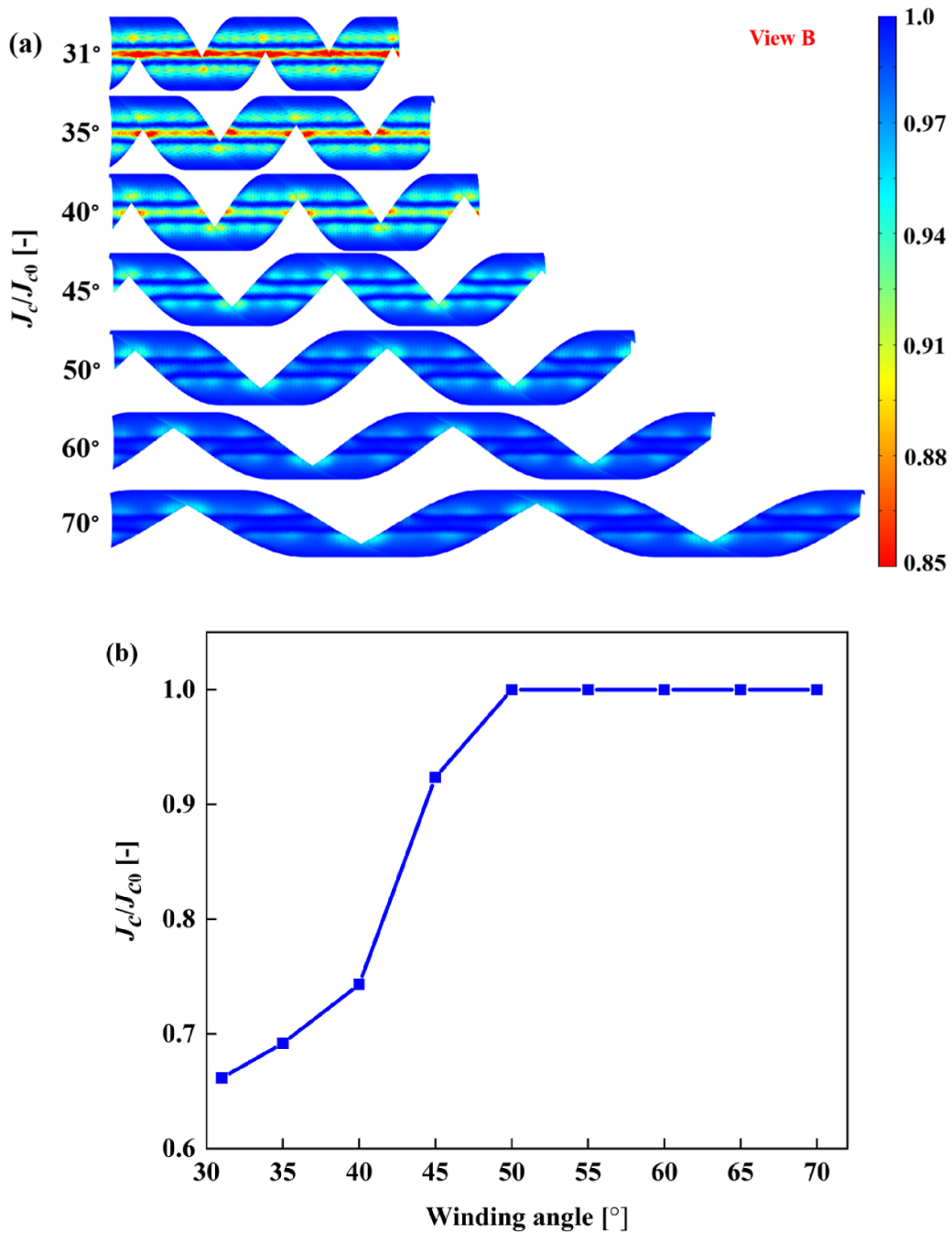
Figure 10. Critical current reduction with winding angle after the transverse compressive strain of 5.41% for single-layer CORC cable.

3.3.2. Magnetization loss with applied AC magnetic field and transverse compressive load.
The AC magnetic field affects the distribution and reduction of the critical current of the superconducting material [17, 18, 46], but this effect does not necessarily make the critical current degrade. The critical current reduction of the superconducting tape in the cable varies with the external AC magnetic field amplitude in transverse direction of the cable [47, 48]. The effect of the AC magnetic field on the electromagnetic performance of single-layer CORC cables under transverse compressive load is discussed in this section only, and the effect of transport current is not specifically analyzed.

The reduction of the critical performance of the ReBCO layer under transverse load is given for a CORC cable with a winding angle of 35 for different periods of a sinusoidal applied magnetic field. As shown in figure 12(a), there is a major effect on the local critical current from the axial strain of the ReBCO layer at the contact area (seen from view B). The critical current becomes further limited in figures 12(c) and (d) for an applied AC field but the transverse compressive
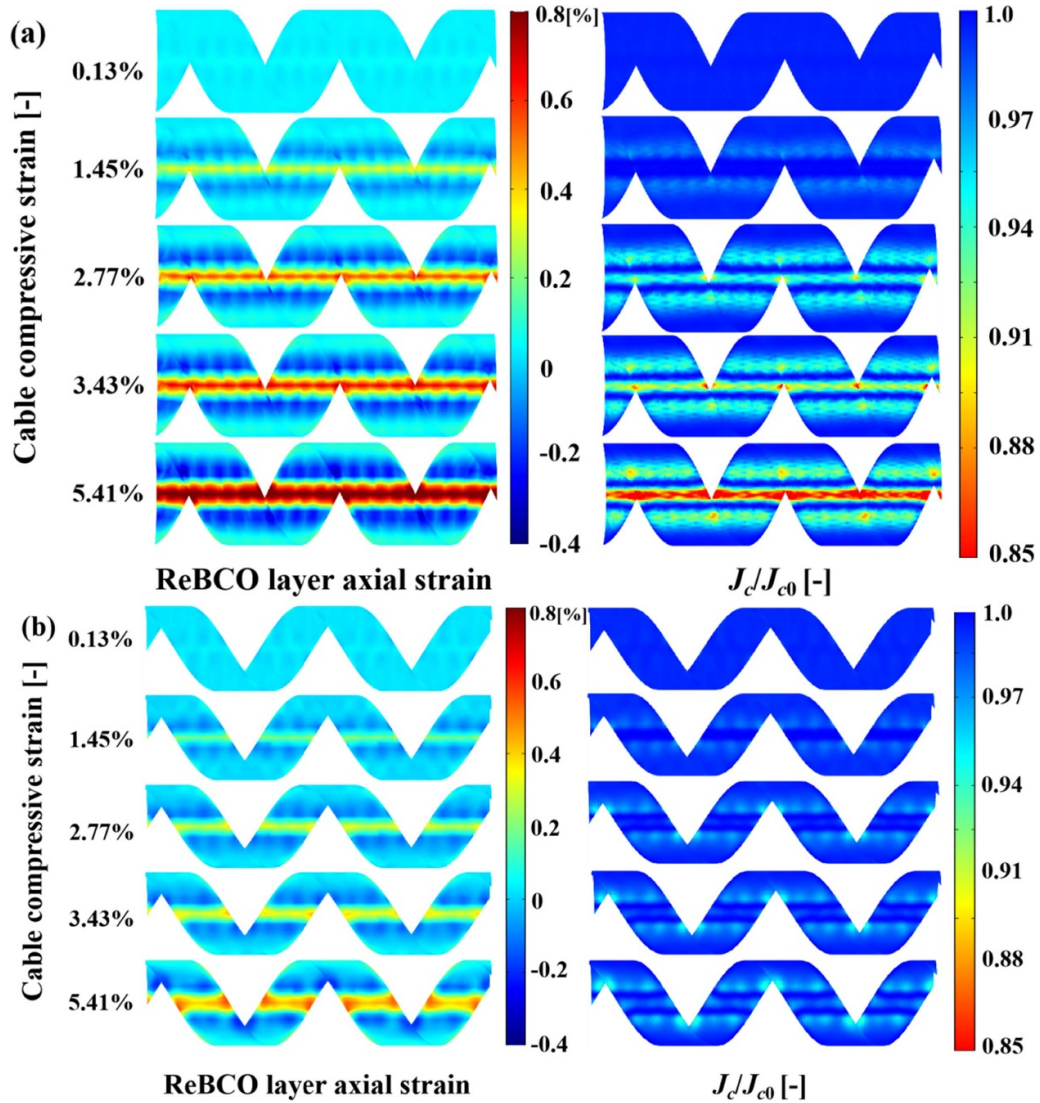
Figure 11. Axial strain distribution and critical current reduction of ReBCO layers for (a) 31 and (b) 50 winding angle of CORC cables at different transverse compressive strains (view B).

strain on the CORC cable does not affect the I_c seen from for view A, since the strain does not change notably for these parts of the tapes. In addition, the reduction of the critical current in the ReBCO layer is most pronounced when the amplitude of the transverse background magnetic field is at the peak and minimum, i.e. when the time is at ($1/4$ cycles and $3/4$ cycles) and dB/dt is zero. Even when the amplitude of the transverse AC magnetic field is zero at $1/2$ cycles and 1 cycles, the induced magnetic self-field generated by the induced currents in the ReBCO layer is still present. This induced magnetic self-field causes the reduction of the critical current.

In the previous part, we mentioned that the critical current reduction of the ReBCO layer in the non-contact area is not significant when the transverse compressive strain of the CORC cable changes with applied AC magnetic field. Based on this, the axial strains of the ReBCO layer are shown in figure 13. The cloud diagram shows that the axial strain of the ReBCO layer in the non-contact area does not vary

much with the transverse compressive load, so the critical current reduction is not significant. Note that the axial strain of the ReBCO layer in the non-contact area decreases slightly with increasing transverse compressive load, which the interaction by core support may cause. To verify this conjecture, we removed the winding core in the model. The cloud of the axial strain of the tape and the ReBCO layer for different transverse compression strains are obtained and shown in figure 14. As shown in figure 14(a), the axial strain in the ReBCO layer in the non-contact area of the CORC cable with no winding core becomes more compressive with increasing transverse compressive strain. The axial strain of the ReBCO layer in the non-contact area of the CORC cable with the presence of a winding core increases positively with the transverse compression strain, as shown in figure 14(b). Therefore, the CORC cable with a winding core can prevent the negative growth of ReBCO layer strain of the non-contact area when the transverse compressive strain increases. In addition, the axial
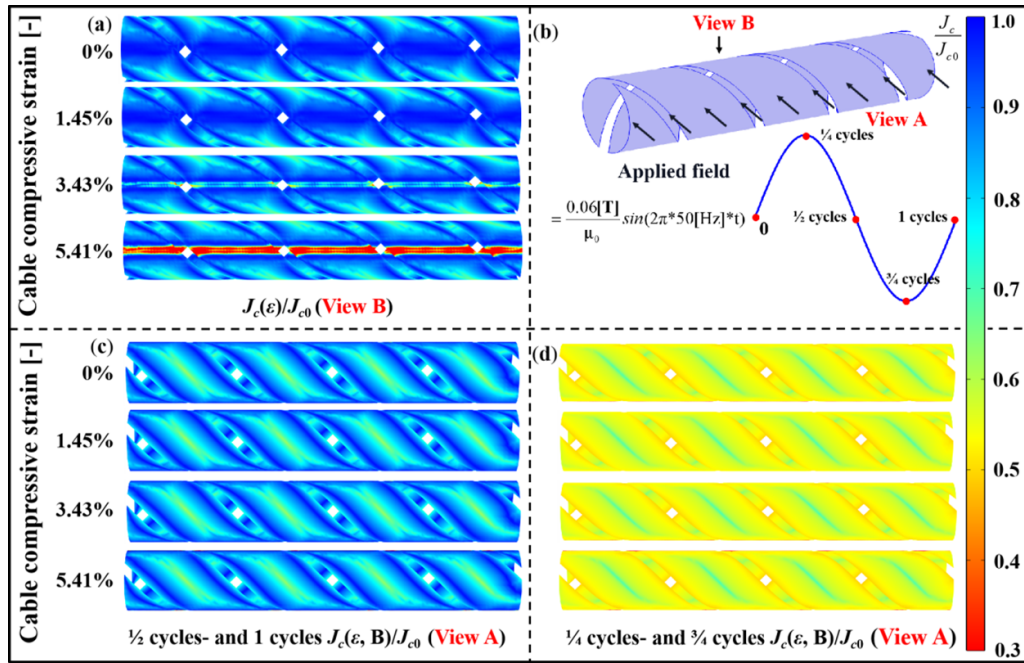
Figure 12. The critical current reduction of the ReBCO layer in the CORC cable under the combined effect of transverse compressive strain and applied magnetic field.
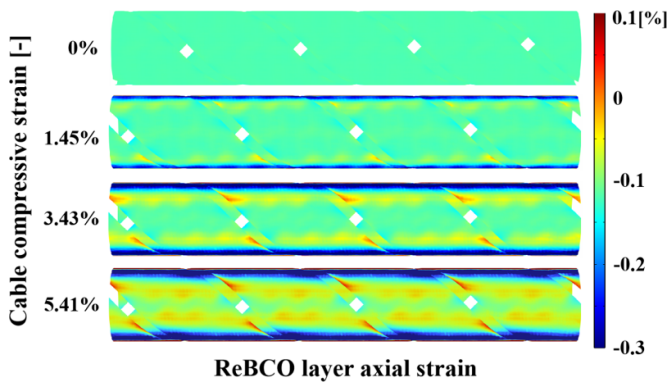

Figure 13. The strain distribution of ReBCO layers of CORC cables, made with a 35° winding angle, under different transverse compressive strains (view A).

strain of the ReBCO layer in the non-contact area in figure 13 is negative and tends to zero as the transverse compressive strain increases. It is mainly due to the initial thermal strain of -0.15% factored into the CORC cable electromagnetic analysis.

Figure 15 depicts the magnetization loss in the tape for four different winding angles for CORC cables under different transverse compressive strains. It should be noted here that all the mentioned magnetization loss refers to the magnetization loss of the tape. The magnetization loss of the winding core, i.e. eddy current loss, is not involved in this paper. The eddy current loss of different CORC cable core materials is detailed in [49]. Only the CORC cable pitch changes when the winding angle changes, so we use the unit cable length to express the magnetization loss instead of the unit

volume. The magnetization loss per unit length of cable is almost unchanged when the transverse compression strain of the cable is small. As the transverse compression strain of the cable increases, the smaller the winding angle of the CORC cable, the more the magnetization loss increases. For example, when the transverse compression strain exceeds 2.11%, the magnetization loss per unit length of the CORC cable with a 31 winding angle increases fast. The magnetization loss per unit length of cable for CORC cables with a winding angle of 40 increases rapidly only when the transverse compression strain exceeds 4.49%. However, the magnetization loss per unit length does not increase for the 45 winding angle CORC cable, even with a transverse compression strain of 5.41%. It can be seen from figure 15 that the axial strain of the ReBCO layer in the non-contact area has a considerable effect on the magnetization loss per unit length of cable. The smaller the axial strain in the ReBCO layer in the non-contact area, the less the irreversible critical current reduction caused by mechanical deformation, resulting in a higher induced current density and a significant increase in magnetization loss. Therefore, when transverse compressive strain reaches a particular level (this particular level is related to the winding angle and increases with the winding angle), magnetization loss appears to increase abruptly. Smaller winding angles cause increased magnetization loss per unit cable length because more pitch per unit length of cable is exposed to the magnetic field.

The magnetization loss per unit length of a single-layer CORC cable after subjecting to a 5.41% transverse compressive strain with different background field amplitudes is shown in figure 16. The magnetization loss increases approximately linearly with the magnetic field amplitude. The linearity
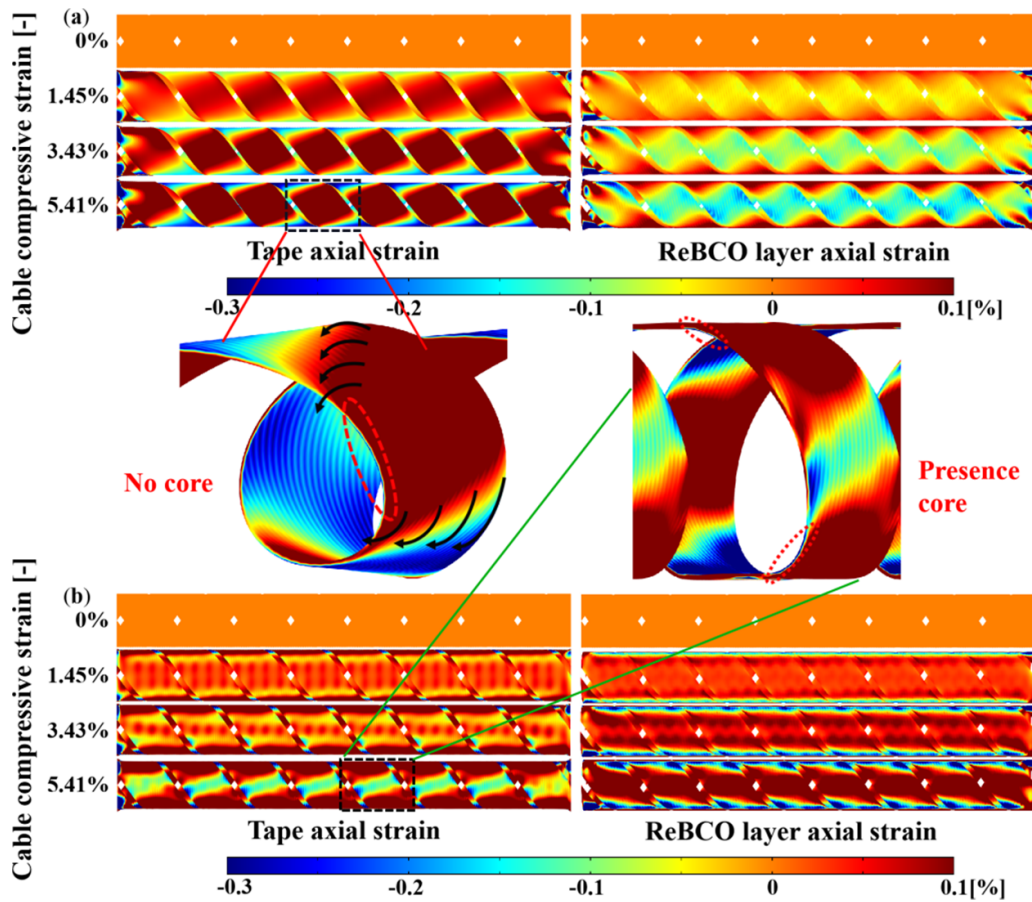
Figure 14. The axial strain distribution of the tape and ReBCO layer of CORC cables made without (a) and with (b) winding core at a winding angle of 35, after a transverse compressive strain of 5.41%.
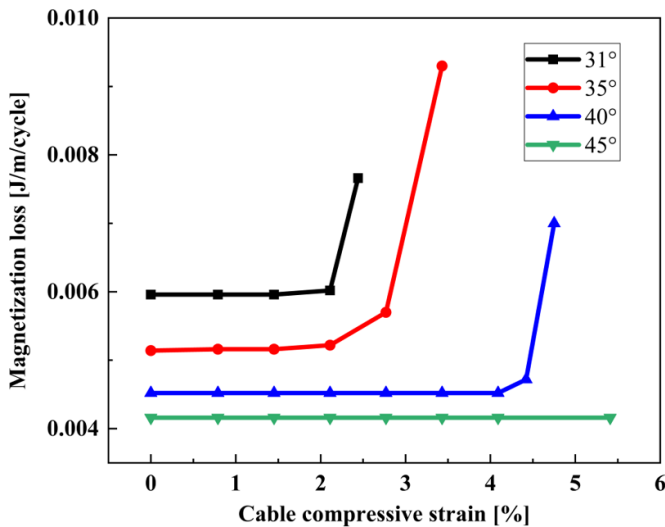

Figure 15. Magnetization loss as a function of winding angles of single-layer CORC cables, applied different cable transverse compressive strain.
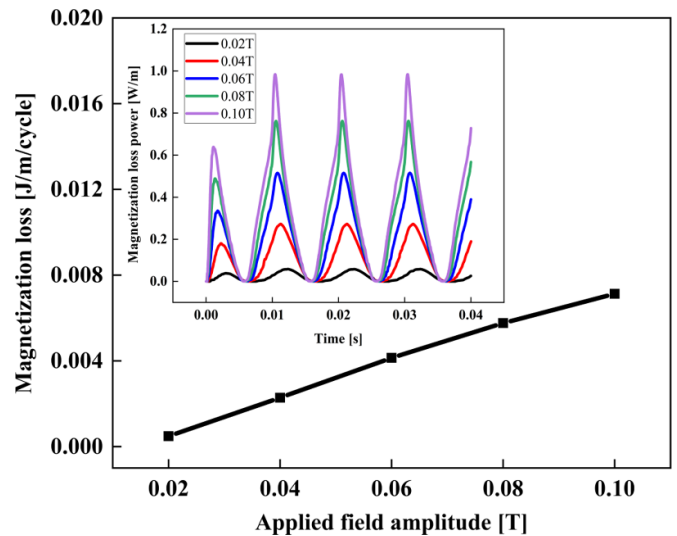

Figure 16. Magnetization loss distribution among single-layer CORC cable with different background magnetic field amplitudes, applied cable transverse compressive strain of 5.41%.

increase may be because the helical structure of the CORC cable penetration field lower than the straight tape. After all, the helical tape of the CORC cable has an angle with the external magnetic field everywhere, not always 90°. Secondly,

the transverse load applied to the CORC cable causes the tape critical current reduction, which also leads to a decrease in the penetration field of the CORC cable. From the figure, it can also be seen that this penetration field is lower than 0.02 T.
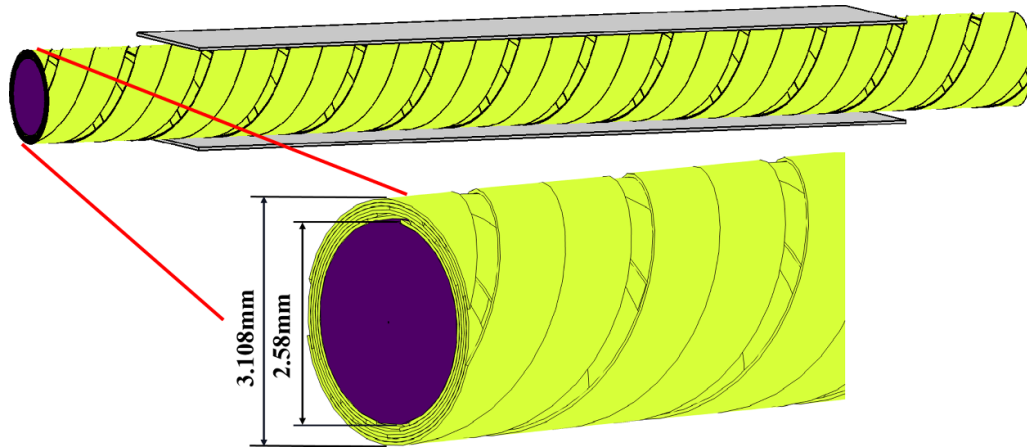
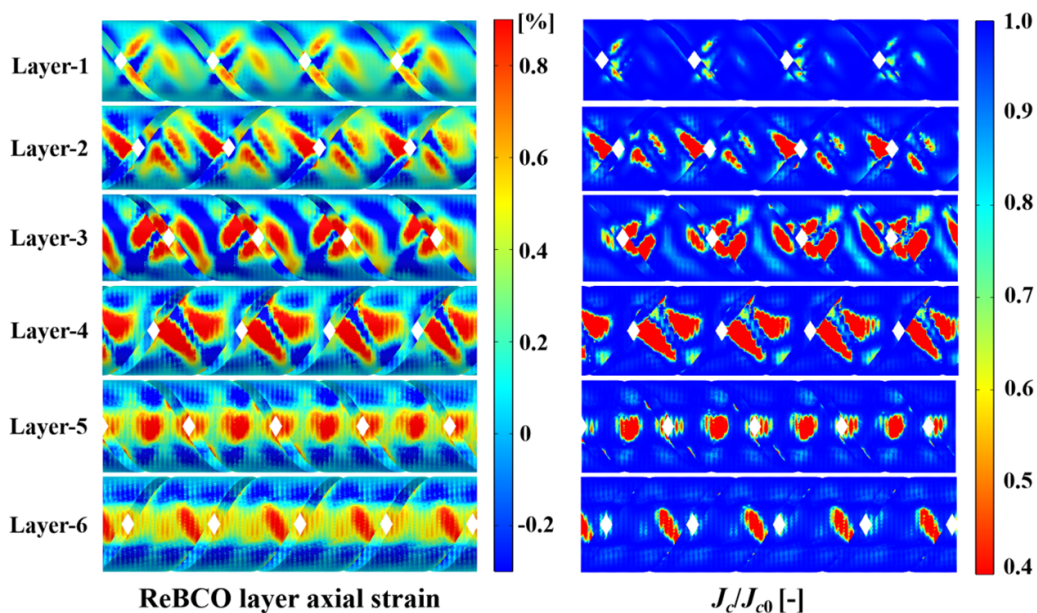**Figure 17.** Model schematic of a six-layer CORC cable.

Figure 18. Axial strain distribution and critical current degradation of a six-layer CORC cable after a cable transverse compressive strain of 18.6%.

However, no expression can calculate the penetration field of CORC cables until now.

For the case of combined transverse load and AC magnetic field, the CORC cable with larger angle winding has not only the ability to withstand better transverse deformation but also has relatively low magnetization loss per unit length of CORC cable. This is useful for CORC cables requiring smaller losses in high-energy physics and energy conversion applications.

3.4. Multiple-layer structure CORC cables

After discussing the analysis of the electromagnetic behavior of single-layer under transverse compressive loads, we further discuss the case of more multiple-layer CORC cables. Unlike single-layer CORC cables, multiple-layer CORC cables have a more complex structure that also requires the consideration of inter-layer interactions. Our study is based on a six-layer

example since the 12-layer CORC cable is computationally very challenging. Figure 17 shows a schematic of the model built using six-layer CORC cable parameters produced by Advanced Conductor Technologies LLC (ACT). Details of the CORC® wire structure are explained in [50] and the tape type is SCS2030 from Superpower Inc.

Figure 18 show the axial strain distribution and critical current reduction characteristics of the ReBCO layers for a six-layer CORC cable following an 18.6% transverse compressive strain. The degradation of the critical current is smallest in the innermost layer and greatest in the middle layer. It is mainly due to the effect of transverse compressive load and the interaction between the layers resulting in the highest strain in the middle layer of the CORC cable and relatively low strain in the innermost and outermost layers. Further, we analyzed the critical current reduction in each of the six layers of the CORC cable under different transverse compression strains.
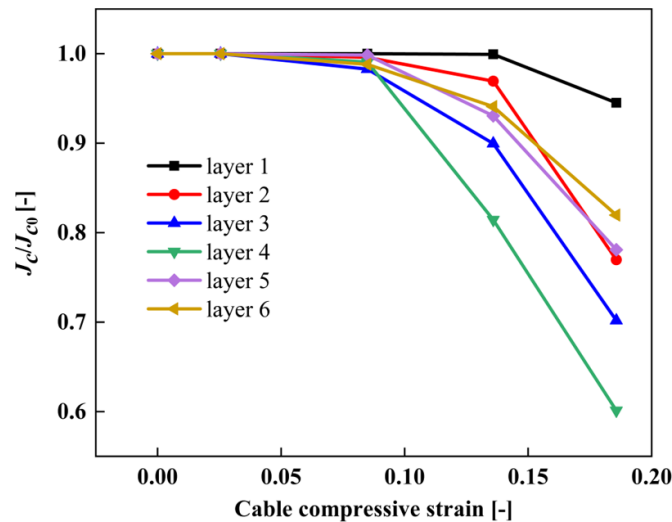
Figure 19. Critical current reduction as a function of applied cable compressive strain of six-layer CORC cable.
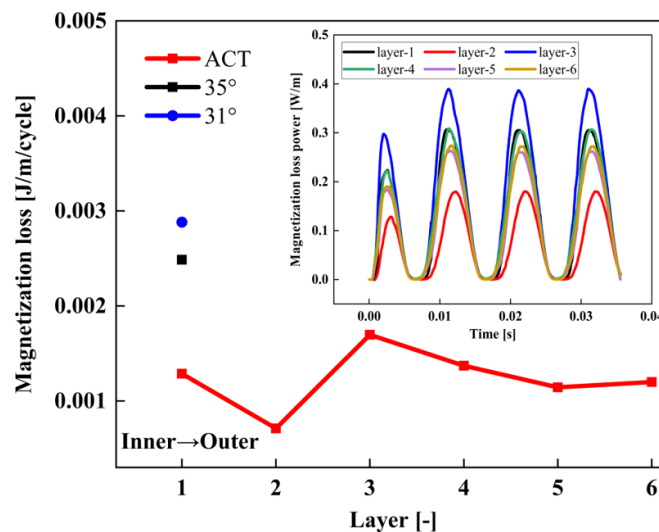

Figure 20. Magnetization loss distribution among single-layer and six-layers of CORC cable for an applied field amplitude of 0.05 T.

As shown in figure 19, the critical currents of the layers hardly reduce when the transverse compressive strain does not exceed 10%. The critical current starts to reduce only when the transverse compression strain of the cable exceeds about 3% for single-layer CORC cables with a winding angle of 35. It indicates that a multi-layer CORC cable can resist large transverse compression loads compared to a single layer cable. The critical currents of each layer show different degrees of degradation with increasing transverse compressive strain, but the middle layers degrade the fastest.

Further, we discuss the effect of an applied AC magnetic field on the magnetization loss of the six-layer CORC cable. Figure 20 gives the magnetization loss power and energy per unit length of CORC cable when the cable is in a no-strain condition, with a transverse sinusoidal magnetic field only. The magnetization loss shows an approximately uniform distribution among the six layers of the cable. Only the extremes appear in the second and third layers, respectively. This is

likely because ACT produced the six-layer CORC cable with the winding angle of each layer approximately between 30 and 36. Therefore, we compared the magnetization loss per unit length of single-layer CORC cables with winding angles of 31 and 35. As shown in the blue and black dots in figure 20, it is clear that the magnetization loss of a single-layer CORC cable is higher than that of a six-layer CORC cable. Overlapped ReBCO tapes have field shielding effects with the same applied field, resulting in less magnetization loss on each tape in a six-layer CORC cable. To reflect on this phenomenon more clearly, we show the current density for a single-layer CORC cable with a winding angle of 35 and each layer of a six-layer CORC cable in figure 21. Two large magnetization current loops are induced on the single-layer tape within a pitch. In six-layer CORC cables, the induced magnetization current is divided into many small local current loops due to the magnetic shielding effect between the overlapping ReBCO bands. Therefore, the induced current on each tape in the six-layer
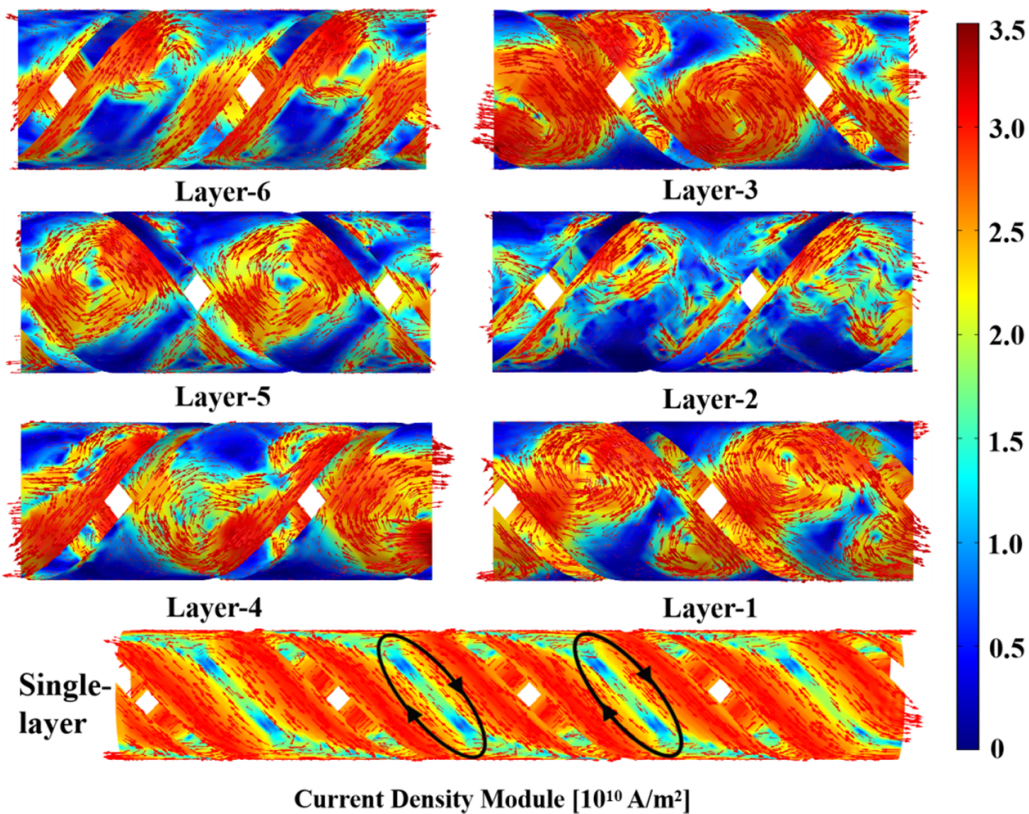
Figure 21. The induced current density distribution in the single-layer and six-layers CORC cables, at t = 1 cycles and with an applied field amplitude of 0.05 T.

CORC cable is smaller, and the magnetization loss is also smaller.

The above results show that for multilayer CORC cables, a reasonable design is one in which the winding angles of each layer in the cable do not differ much, and the winding directions of adjacent layers are opposite [17]. This can result in relatively low magnetization losses that are uniformly distributed among the layers and can resist relatively high transverse loads.

4. Conclusion

A detailed CORC cable mechanical-electromagnetic FE model is developed to analyze the electromagnetic characteristics under transverse compressive loading. The transverse load is to simulate the real existing electromagnetic force. The CORC transverse loading FE model can reasonably predict the CORC cable performance. The FE model results show that the smaller the winding angle, the greater the axial strain and critical current reduction of the ReBCO layer is in the contact area. Poisson's ratio and wound core size have almost no effect on the ReBCO layer strain. The presence of the winding core causes the strain in the non-contact area of the ReBCO layer to change from zero to a positive increase when the transverse compressive load increases. Multilayer CORC cable calculation results show that the axial strain and critical current reduction are the smallest in the innermost layer and most significant in the middle layer. In the zero applied strain case, the magnetization loss per unit cable length is approximately uniformly distributed for each six-layer CORC cable. Compared to single-layer CORC cables with winding angles of 31 and 35, the magnetization loss is lower for each layer of the CORC cable than for single-layer CORC. The developed models can serve in the design optimization of CORC cables.

Data availability statement

All data that support the findings of this study are included within the article (and any supplementary files).

ORCID iDs

Jiangtao Yan ⬤ https://orcid.org/0000-0003-1924-8404
Keyang Wang ⬤ https://orcid.org/0000-0001-5858-5396
Yuanwen Gao ⬤ https://orcid.org/0000-0002-9536-0070
Arend Nijhuis ⬤ https://orcid.org/0000-0002-1600-9451

References

[1] Obradors X and Puig T 2014 Coated conductors for power applications: materials challenges *Supercond. Sci. Technol.* **27** 044003

[2] Mitchell N *et al* 2021 Superconductors for fusion: a roadmap *Supercond. Sci. Technol.* **34** 103001

[3] Zhai Y, van der Laan D, Connolly P and Kessel C 2021 Conceptual design of HTS magnets for fusion nuclear science facility *Fusion Eng. Des.* **168** 112611

[4] Bai H *et al* 2020 The 40 T superconducting magnet project at the National High Magnetic Field Laboratory *IEEE Trans. Appl. Supercond.* **30** 4300405

[5] Maeda H and Yanagisawa Y 2014 Recent developments in high-temperature superconducting magnet technology *IEEE Trans. Appl. Supercond.* **24** 4602412

[6] Hu X *et al* 2020 Analyses of the plastic deformation of coated conductors deconstructed from ultra-high field test coils *Supercond. Sci. Technol.* **33** 095012

[7] Zhang X, Sun C, Liu C and Zhou Y 2020 A standardized measurement method and data analysis for the delamination strengths of YBCO coated conductors *Supercond. Sci. Technol.* **33** 035005

[8] Anvar V A *et al* 2018 Bending of CORC® cables and wires: finite element parametric study and experimental validation *Supercond. Sci. Technol.* **31** 115006

[9] Anvar V A, Wang K, Weiss J D, Radcliff K, van der Laan D C, Hossain M S A and Nijhuis A 2022 Enhanced critical axial tensile strain limit of CORC® wires: FEM and analytical modeling *Supercond. Sci. Technol.* **35** 055002

[10] Wang K, Gao Y, Luo W, Zhou Y H and Nijhuis A 2021 Nonlinear contact behavior of HTS tapes during pancake coiling and CORC cabling *Supercond. Sci. Technol.* **34** 075003

[11] Wang K, Gao Y W, Anvar V A, Radcliff K, Weiss J D, van der Laan D C, Zhou Y H and Nijhuis A 2022 Prediction of strain, inter-layer interaction and critical current in CORC® wires under axial strain by T-A modeling *Supercond. Sci. Technol.* **35** 105012

[12] van der Laan D C, Radcliff K, Anvar V A, Wang K, Nijhuis A and Weiss J D 2021 High-temperature superconducting CORC® wires with record-breaking axial tensile strain tolerance present a breakthrough for high-field magnets *Supercond. Sci. Technol.* **34** 10LT01

[13] Mulder T 2018 Advancing ReBCO-CORC wire and cable-in-conduit conductor technology for superconducting magnets *PhD Thesis* University of Twente (https://doi.org/10.3990/1.9789036546164)

[14] van der Laan D C, McRae D M and Weiss J D 2019 Effect of monotonic and cyclic axial tensile stress on the performance of superconducting CORC® wires *Supercond. Sci. Technol.* **32** 054004

[15] Solovyov M, Šouc J and Gömöry F 2014 AC loss properties of single-layer CORC cables *J. Phys.: Conf. Ser.* **507** 022034

[16] Sheng J, Vojenciak M, Terzioglu R, Frolek L and Gömöry F 2017 Numerical study on magnetization characteristics of superconducting conductor on round core cables *IEEE Trans. Appl. Supercond.* **27** 4800305

[17] Wang Y, Zhang M, Grilli F, Zhu Z and Yuan W 2019 Study of the magnetization loss of CORC cables using a 3D T-A formulation *Supercond. Sci. Technol.* **32** 025003

[18] Wu Q, Wang Y, Huang Z, Xie Y, He R, Wei J, Lei Z, Qin J and Tan Y 2022 Electromagnetic and mechanical properties of CORC cable due to screening current *Supercond. Sci. Technol.* **35** 075005

[19] Clegg M, Kapolka M and Ruiz H S 2022 Impact of the magneto angular dependence of the critical current density in CORC cables *IEEE Trans. Appl. Supercond.* **32** 6600906

[20] Li X *et al* 2021 Calculation of CORC cable loss using a coupled electromagnetic-thermal T-A formulation model *IEEE Trans. Appl. Supercond.* **31** 4802707

[21] Fareed M U, Kapolka M, Robert B C, Clegg M and Ruiz H S 2022 3D modelling and validation of the optimal pitch in commercial CORC cables *IOP Conf. Ser.: Mater. Sci. Eng.* **1241** 012030

[22] van der Laan D C, Mcrae D M and Weiss J D 2019 Effect of transverse compressive monotonic and cyclic loading on the performance of superconducting CORC® cables and wires *Supercond. Sci. Technol.* **32** 015002

[23] Hong Z, Campbell A M and Coombs T A 2006 Numerical solution of critical state in superconductivity by finite element software *Supercond. Sci. Technol.* **19** 1246–52

[24] Shen B, Grilli F and Coombs T 2020 Review of the AC loss computation for HTS using H formulation *Supercond. Sci. Technol.* **33** 033002

[25] Zhang H M, Zhang M and Yuan W J 2017 An efficient 3D finite element method model based on the T-A formulation for superconducting coated conductors *Supercond. Sci. Technol.* **30** 024005

[26] Berrospe-Juarez E, Zermeño V M R, Trillaud F and Grilli F 2019 Real-time simulation of large-scale HTS systems: multi-scale and homogeneous models using the T-A formulation *Supercond. Sci. Technol.* **32** 065003

[27] Vargas-Llanos C R and Grilli F 2021 Homogenization in 3D based on the T-A formulation *7th Int. Workshop on Numerical Modelling of High Temperature Superconductors (Virtual Conf.)*

[28] Mitchell N, Devred A, Larbalestier D C, Lee P J, Sanabria C and Nijhuis A 2013 Reversible and irreversible mechanical effects in real cable-in-conduit conductors *Supercond. Sci. Technol.* **26** 114004

[29] Freund L B and Suresh S 2003 *Thin Film Materials: Stress, Defect Formation, and Surface Evolution* (Cambridge: Cambridge University Press)

[30] Cheon J H, Shankar P S and Singh J P 2005 Influence of processing methods on residual stress evolution in coated conductors *Supercond. Sci. Technol.* **18** 142–6

[31] COMSOL, Inc. Cylinder roller contact (available at: www.comsol.com/model/cylinder-roller-contact-1431) (accessed 11 March 2021)

[32] Liang F, Venuturumilli S, Zhang H, Zhang M, Kvitkovic J, Pamidi S, Wang Y and Yuan W 2017 A finite element model for simulating second generation high temperature superconducting coils/stacks with large number of turns *J. Appl. Phys.* **122** 043903

[33] Wang Y, Bai H, Li J, Zhang M and Yuan W 2020 Electromagnetic modelling using T-A formulation for high-temperature superconductor $(RE)Ba_2Cu_3O_X$ high field magnets *High Volt.* **5** 218–26

[34] Berrospe-Juarez E, Trillaud F, Zermeno V M R, Grilli F, Weijers H W and Bird M D 2020 Screening currents and hysteresis losses in the REBCO insert of the 32 T all-superconducting magnet using T-A homogenous model *IEEE Trans. Appl. Supercond.* **30** 4600705

[35] Grilli F, Sirois F, Zermeno V M R and Vojenciak M 2014 Self-consistent modeling of the I_c of HTS devices: how accurate do models really need to be? *IEEE Trans. Appl. Supercond.* **24** 8000508

[36] Barth C, Mondonico G and Senatore C 2015 Electro-mechanical properties of REBCO coated conductors from various industrial manufacturers at 77 K, self-field and 4.2 K, 19 T *Supercond. Sci. Technol.* **28** 045011

[37] van der Laan D C and Ekin J W 2007 Large intrinsic effect of axial strain on the critical current of high-temperature superconductors for electric power applications *Appl. Phys. Lett.* **90** 052506

[38] Kajikawa K, Hayashi T, Yoshida R, Iwakuma M and Funaki K 2003 Numerical evaluation of AC losses in HTS wires with 2D FEM formulated by self magnetic field *IEEE Trans. Appl. Supercond.* **13** 3630–3

[39] Zermeno V M R, Abrahamsen A B, Mijatovic N, Jensen B B and Sorensen M P 2013 Calculation of alternating current losses in stacks and coils made of second generation high temperature superconducting tapes for large scale applications *J. Appl. Phys.* **114** 173901

[40] Wang Y, Song H, Yuan W, Jin Z and Hong Z 2017 Ramping turn-to-turn loss and magnetization loss of a no-insulation (Re) Ba$_2$Cu$_3$O$_x$ high temperature superconductor pancake coil *J. Appl. Phys.* **121** 113903

[41] Queval L, Zermeno V M R and Grilli F 2016 Numerical models for AC loss calculation in large-scale applications of HTS coated conductors *Supercond. Sci. Technol.* **29** 024007

[42] Jiang Z, Zhou W, Li Q, Yao M, Fang J, Amemiya N and Bumby C B 2018 The dynamic resistance of YBCO coated conductor wire: effect of DC current magnitude and applied field orientation *Supercond. Sci. Technol.* **31** 035002

[43] llin K, Yagotintsev K A, Zhou C, Gao P, Kosse J, Otten S J, Wessel W A J, Haugan T J, van der Laan D C and Nijhuis A 2015 Experiments and FE modeling of stress–strain state in ReBCO tape under tensile, torsional and transverse load *Supercond. Sci. Technol.* **28** 055006

[44] Wang Y, Zheng J, Zhu Z, Zhang M and Yuan W 2019 Quench behavior of high temperature superconductor (Re)Ba$_2$Cu$_3$O$_x$ CORC cable *J. Phys. D: Appl. Phys.* **52** 345303

[45] Phifer V, Small M, Bradford G, Weiss J, van der Laan D and Cooley L 2022 Investigations in the tape-to-tape contact resistance and contact composition in superconducting CORC® wires *Supercond. Sci. Technol.* **35** 065003

[46] van der Laan D C, Noyes P D, Miller G E, Weijers H W and Willering G P 2013 Characterization of a high-temperature superconducting conductor on round core cables in magnetic fields up to 20 T *Supercond. Sci. Technol.* **26** 045005

[47] Rabbers J J *et al* 1999 Magnetisation and transport current loss of a BSCCO/Ag tape in an external AC magnetic field *IEEE Trans. Appl. Supercond.* **9** 2382414

[48] Hao L *et al* 2022 Conceptual design and optimisation of HTS Roebel tapes *IEEE Trans. Appl. Supercond.* **32** 5900505

[49] Ye H, Li W, Li Z, Li X, Jin Z and Sheng J 2020 Effect of core materials on the electrical properties of superconducting conductor on round core cable *IEEE Trans. Appl. Supercond.* **30** 2968257

[50] Weiss J D, Mulder T, ten Kate H J and van der Laan D C 2016 Introduction of CORC® wires: highly flexible, round high-temperature superconducting wires for magnet and power transmission applications *Supercond. Sci. Technol.* **30** 014002